PCCP

PAPER

View Article Online
View Journal | View Issue

Cite this: *Phys. Chem. Chem. Phys.*, 2017, **19**, 30147

Molecular stacking effect on photoluminescence quantum yield and charge mobility of organic semiconductors†

Jianzhong Fan, Lili Lin* and Chuan-Kui Wang*

Received 10th August 2017,
Accepted 17th October 2017

DOI: 10.1039/c7cp05451c

rsc.li/pccp

The photoluminescence quantum yield (PLQY) and charge transfer property of the high mobility emissive organic semiconductors, 2,6-diphenylanthracene (DPA) and 2,6-diphenyl-9,10-bis(phenylethynyl)anthracene (DP-BPEA), are theoretically investigated. A quantum mechanics/molecular mechanics (QM/MM) method is adopted to investigate the photophysical properties, the Marcus equation is used to describe hole and electron transfer rates, and kinetic Monte Carlo simulation is performed to obtain charge mobility. In both solution and solid phase, the PLQY and the charge mobility of DPA and DP-BPEA are calculated, and the molecular stacking effect is analyzed. For DPA, the rotation motions of the terminal phenyl ring are obviously restricted in the solid phase, which results in the decrease of the Huang–Rhys factor and reorganization energy. This restricted intramolecular rotation (RIR) effect suppresses dissipation pathways of the excited state energy. As a result, the aggregation induced enhancement emission (AIEE) is thus revealed for this emitter from the tetrahydrofuran (THF) solution to the solid phase. However for DP-BPEA, the geometrical variations between the ground and excited states are almost unchanged from the THF solution to the solid phase, and only a restricted intramolecular vibration (RIV) of bond length (*e.g.* –C≡C–) is displayed. As RIV is not obvious as RIR, a similar fluorescence efficiency is obtained for DP-BPEA in THF solution and the solid phase. In addition, DPA and DP-BPEA crystals are proven to be p-type semiconductors. The calculated mobility of the hole for DPA (3.39 $cm^2 V^{-1} s^{-1}$) is larger than that of DP-BPEA (1.62 $cm^2 V^{-1} s^{-1}$) because the number of effective transition pathways of DPA is more than that of DP-BPEA. Our study demonstrates that the different molecular stacking of organic semiconductors has an important effect on their photophysical and charge transfer properties.

1. Introduction

Organic optoelectronic devices based on organic semiconductors such as organic light emitting diodes (OLEDs), organic field effect transistors (OFETs) and organic photovoltaics (OPVs), have been greatly developed due to their promising application in flexible displays and solid-state lighting sources.[1–5] Recently, organic light emitting transistors (OLETs) with the characteristics of OLED (efficient emitting) and OFET (high mobility) have shown great potential application in integrated circuit signal processing and all organic active matrix flexible displays.[6–10] To fulfil the demands of the promising device structure, developing an organic semiconductor with efficient emission and high charge mobility is desired, and the molecular stacking model (aggregated structure) plays a key role in determining the properties of the materials.[11,12] For OFETs, the H-aggregation which can provide a large transfer integral (V) is pursued for realizing high mobility. However for OLEDs, the X-aggregation is expected for preventing the aggregation induced fluorescence quenching. So, balancing intermolecular stacking (for efficient charge transfer) and nonradiative energy transfer (for efficient emission) remains a challenge for the achievement of organic semiconductors with both a high mobility and strong fluorescence emission.

Recently, Hu *et al.* have synthesized the high mobility organic semiconductor, 2,6-diphenylanthracene (DPA), which is shown in Fig. 1a with a strong blue emission.[13] In single crystals, the mobility is as high as 34 $cm^2 V^{-1} s^{-1}$ and the photoluminescence quantum yield (PLQY) is 41.2%. OLEDs and OFETs are fabricated with DPA, and this is the first time that the possibility of integration of optoelectronic devices based on the same organic semiconductor has been realized, indicating the potential of DPA in organic optoelectronics especially planar integration. Based on the DPA structure, they

Shandong Province Key Laboratory of Medical Physics and Image Processing Technology, Institute of Materials and Clean Energy, School of Physics and Electronics, Shandong Normal University, 250014 Jinan, China.
E-mail: ckwang@sdnu.edu.cn, linll@sdnu.edu.cn

† Electronic supplementary information (ESI) available. See DOI: 10.1039/c7cp05451c

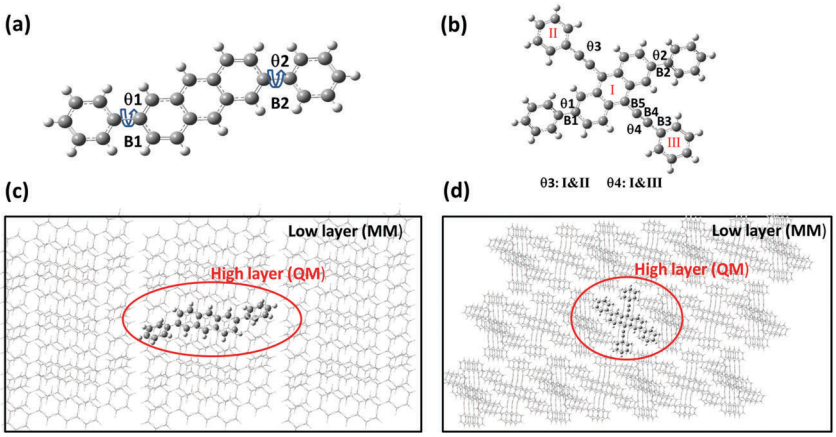

Fig. 1 Chemical structure of DPA (a) and DP-BPEA (b). QM/MM model for DPA (c) and DP-BPEA (d): the single centered molecule is treated as the high layer and its surrounding molecules are regarded as the low layer.

designed another organic semiconductor 2,6-diphenyl-9,10-bis-(phenylethynyl)anthracene DP-BPEA (shown in Fig. 1b) with fluorescence efficiency of 32% and mobility of 1.37 $cm^2\ V^{-1}\ s^{-1}$.[14] Thus, theoretical investigations to explore the relationship between molecular stacking and light emitting efficiency as well as the charge transport property for DPA and DP-BPEA in the solid phase are necessary to reveal the inner mechanism and further develop more efficient organic semiconductors for OLEDs, OFETs and OLETs.

In this work, we adopt a quantum mechanics/molecular mechanics (QM/MM) method with the multimode coupled thermal vibration correlation function (TVCF) formalism to study the luminescence property in the solid phase.[15,16] For charge transport properties, the hole and electron transfer rates are calculated by the Marcus equation and the mobility is thus obtained by kinetic Monte Carlo simulation.[17,18] Our theoretical work clearly demonstrates the influence of different molecular stacking on light emitting efficiency and charge mobility.

2. Theoretical method

According to the Jablonski diagram, there are three major de-excitation pathways for the first singlet excited state (S1): one is the radiative decay from S1 to the ground state (S0) with the rate k_r, second is the nonradiative decay internal conversion from S1 to S0 with the rate k_{IC}, and the third is the intersystem crossing (ISC) from S1 to the first triplet excited state (T1) with the rate k_{ISC}. Thus, the fluorescence quantum yield (Φ_F) can be expressed as $\Phi_F = \frac{k_r}{k_r + k_{nr}} = \frac{k_r}{k_r + k_{IC} + k_{ISC}}$. In this work k_{ISC} is neglected because it is very small for organic molecules with a $\pi \rightarrow \pi^*$ transition nature. Therefore, either suppressing the nonradiative decay internal conversion rate or increasing the radiative decay rate can attain a higher fluorescence efficiency. Moreover, the charge transfer rates of electrons and holes in DPA and DP-BPEA crystals are theoretically calculated based on Marcus theory. Then kinetic Monte Carlo simulation approach is adopted to investigate the charge diffusion process, and further the charge mobility can be acquired.

2.1 Radiative and nonradiative decay rates

The radiative decay rate can be approximately computed by the Einstein spontaneous emission equation $k_r = \frac{f\Delta E_{fi}^2}{1.499}$ where f is the oscillator strength and ΔE_{fi} is the vertical emission energy with the unit of wavenumber (cm^{-1}).

Following Fermi's golden rule, the nonradiative decay internal conversion rate from S1 to S0 can be written as

$$k_{IC} = \frac{2\pi}{\hbar^2}\sum_{u,v} P_{iv}\left|H_{fu,iv}\right|^2 \delta\left(E_{iv} - E_{fu}\right). \quad (1)$$

Here H is the interaction between two different Born–Oppenheimer states, and it contains two contributions as $\hat{H}\Psi_{iv} = \hat{H}^{BO}\Phi_i(r, Q)\Theta_v(Q) + \hat{H}^{SO}\Phi_i(r, Q)\Theta_v(Q)$. Where $\hat{H}^{BO}$ denotes the nonadiabatic coupling and $\hat{H}^{SO}$ is the spin–orbit coupling. Finally, the equation can be written as follows by applying the Fourier transform of the delta function

$$k_{IC} = \sum_{kl}\frac{1}{\hbar^2}R_{kl}\int_{-\infty}^{\infty} dt\left[e^{i\omega_{if}t}Z_i^{-1}\rho_{IC}(t, T)\right]. \quad (2)$$

Here $R_{kl} = \langle\Phi_f|\hat{P}_{fk}|\Phi_i\rangle\langle\Phi_i|\hat{P}_{fl}|\Phi_f\rangle$ is the nonadiabatic electronic coupling. Z_i is the partition function and $\rho_{IC}(t,T)$ is the thermal vibration correlation function (TVCF). $\hat{P}_{fk} = -i\hbar\frac{\partial}{\partial Q_{fk}}$ represents the normal momentum operator of the kth normal mode in the final electronic state. Both the methodology and application of these formalisms can be found in Peng's and Shuai's studies.[19,20]

2.2 Charge transfer rate and charge mobility

As for the charge transfer rate, it can be calculated by Marcus theory

$$k = \frac{V^2}{\hbar}\left(\frac{\pi}{\lambda k_B T}\right)^{1/2}\exp\left(\frac{-\lambda}{4k_B T}\right). \quad (3)$$

where k_B is the Boltzmann constant and T is the temperature, V is the transfer integral and λ is the reorganization energy.

Since the contribution of the reorganization energy from the electronic polarization of surrounding molecules is quite small, the environmental factor for the reorganization energy is ignored and only the intra-molecular reorganization energy is evaluated in this work. Based on the microscopic charge transfer rate in the organic molecular single crystal, a kinetic Monte Carlo simulation approach is adopted to investigate the charge diffusion process. By repeating the process thousands of times, we can get thousands of trajectories. The average value of all the trajectories with respect to time maintains a linear relationship. The 10 × 10 × 10 supercell is adopted and the limit time for every track is set as 0.01 ns and 2000 trajectories are chosen to get the average value of the diffusion coefficient D by the equation: $D = \lim_{t\to\infty} \frac{r^2}{2nt}$ where r, t and n represents the average displacement, total time span and the dimension of the charge transport in the crystal respectively. Finally, the charge mobility (μ) is calculated by the Einstein equation: $\mu = \frac{eD}{k_B T}$. For more details please refer to ref. 21.

3. Computational details

As we all know, the excited state properties are sensitive to the functional, so our first step is to select an optimal functional. Consistent with experiment, the tetrahydrofuran (THF) solution is adopted here. Through comparing the experimental emission wavelength (472 nm) of DPA in the device with the data calculated by B3LYP (487.3 nm), PBE0 (472.4 nm) and BMK (444.2 nm) in the solid, the PBE0 functional with the 6-31G(d) basis set is adopted in later calculations for DPA. Besides, the calculated emission wavelength of DP-BPEA is 579.2 nm by PBE0 which also corresponds well with the experimental result (597 nm). Thus, the function of PBE0 is adopted whether in THF or in the solid phase. To clarify the surrounding environment to the molecular photophysical properties, the solvent effect in THF is modelled by using the polarizable continuum model (PCM) and the stacking surrounding in crystal is incorporated by the combined quantum mechanics and molecular mechanics (QM/MM) approach. As for the solid phase, the initial structure is obtained from the X-ray crystal structure detected experimentally, and then, the QM/MM calculation is realized with the ONIOM method through the Gaussian09 package,[22] which has been applied in our previous work.[15] The model consists of two "layers" (shown in Fig. 1c and d): the centered molecule is treated as a high layer and calculated by the quantum mechanical method, the surrounding molecules are treated as the low layer and computed by molecular mechanics with the UFF force field. Besides, the electronic embedding scheme is adopted in the QM/MM treatment. Finally, the normal mode analyses are performed by the DUSHIN program[23] and the nonradiative decay internal conversion rates from S1 to S0 in THF and the solid phase are both calculated in MOMAP (Molecular Materials Property Prediction Package) which has demonstrated superiority in describing and predicting the optical properties of polyatomic molecules.[24–26]

4. Results and discussion.

4.1 Effect of intermolecular interaction on photophysical properties and geometry changes

Based on the X-ray structures of DPA and DP-BPEA, the molecular stacking modes in the singlet crystals are shown in Fig. 2, and the intermolecular interaction is visualized by the reduced density gradient (RDG) function. Intermolecular π–π interactions accompanied by intermolecular noncovalent bonds such as CH–π can be found, different molecular stacking brings about different intermolecular interactions for DPA and DP-BPEA respectively. Although the J-aggregation can be found in two crystals and this

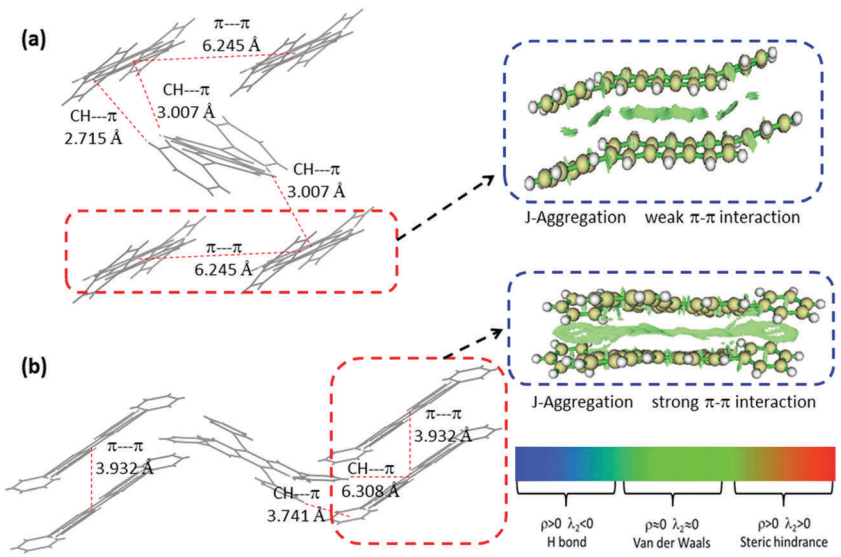

Fig. 2 Molecular packing modes of DPA (a) and DP-BPEA (b) in crystals. The intermolecular interaction is visualized by the reduced density gradient (RDG) function.

stacking mode can balance the contradiction between high mobility and efficient fluorescence emission, a different intermolecular π–π interaction strength is observed for DPA and DP-BPEA due to the unequal distance in the dimer. Besides, the additional phenylethynyl brings about more π–π interaction in the DP-BPEA crystal. To illustrate the effect of the intermolecular interaction on photophysical properties and geometry changes, we firstly performed a geometry optimization for the ground state (S0) and the first excited singlet state (S1) of DPA and DP-BPEA in THF and the solid phase by using PCM and the QM/MM method respectively. The calculated vertical excitation energy (VEE), oscillator strength (f), electric transition dipole moment (EDM) and the assignment for S1 of DPA and DP-BPEA are listed in Tables S1 and S2 (ESI†). It can be seen that S1 is dominated by the transition from the highest occupied molecular orbital (HOMO) to the lowest unoccupied molecular orbital (LUMO) in both THF and the solid phase. The corresponding distributions of HOMO and LUMO as well as their energies are shown in Fig. 3 and Fig. S1 (ESI†). The HOMO is indicative of π character and the LUMO demonstrates the π* feature, which justifies our approximation of neglecting the intersystem crossing process. Besides, for DPA, it can also be seen that the EDM and f become larger in the solid phase than these in THF, and the maximum absorption wavelength is red shifted from THF (399 nm) to the solid phase (412 nm). However for DP-BPEA, the opposite result is found, the EDM and f become smaller in the solid phase than these in THF, and the maximum absorption wavelength blue-shifts from THF (526 nm) to the solid phase (516 nm). These changes indicate that the molecular stacking effect can obviously affect the photophysical properties, and different molecular arrangement characteristics could be identified. Besides, the vibronic resolved UV-vis and fluorescent spectra of DPA and DP-BPEA in THF are shown in Fig. S2 (ESI†). For DPA, as detected in experiment, three absorption peaks 444 nm (0–0), 417 nm (0–1) and 394 nm (0–2) are observed, respectively, and the corresponding emission peaks are 525 nm, 490 nm and 457 nm. As for DP-BPEA, two absorption peaks of 547 nm (0–1) and 592 nm (0–0) are found, and the corresponding emission peaks are 606 nm and 663 nm. Thus, the additional phenylethynyl unit in DP-BPEA can affect the photophysical properties. Moreover, in the case of DP-BPEA in crystal, a red shift and a very broad emission band (500–700 nm) are recorded experimentally. Such a broad emission band should be caused by the presence of different types of solid state excimers rather than the vibronic resolved spectra of the monomer. To demonstrate the reason for the red shift and the very broad fluorescence spectra of DP-BPEA, we calculate the weight spectra of monomer and excimer by the DFT-ONIOM approach with the assumed ratio being 1 : 1, the corresponding result is shown in Fig. S3 (ESI†). The calculated emission wavelength is 579 nm (green line) and 667 nm (blue line) for the monomer and excimer respectively. The weight spectra of the two emissions is shown by the red line, which corresponds well with the experimentally detected very broad and red shifted emission compared with that in solution (633 nm).

For analyzing the effect of molecular stacking on geometry changes, the optimized structure data of DPA and DP-BPEA at both S0 and S1 states in THF and the solid phase are collected in Tables 1 and 2 respectively. The predicted solid phase structure of DPA at S0 is in good agreement with the crystal structure with the calculated θ_1 being 18.7° and experimental value being 20.05°. Good consistency can also be found for DP-BPEA with the calculated θ_1 being 28.9° and experimental value being 28.6°. This indicates the reliability of the adopted QM/MM approach and the selected PBE0 functional. Furthermore, we analyze the structural changes (bond length and dihedral angle) between S0 and S1 in THF and the solid phase for DPA, we know the bond lengths of B_1 and B_2 are weakly changed from the S1 to the S0 state both in THF and the solid phase. However for the dihedral angle of θ_1 and θ_2, they all

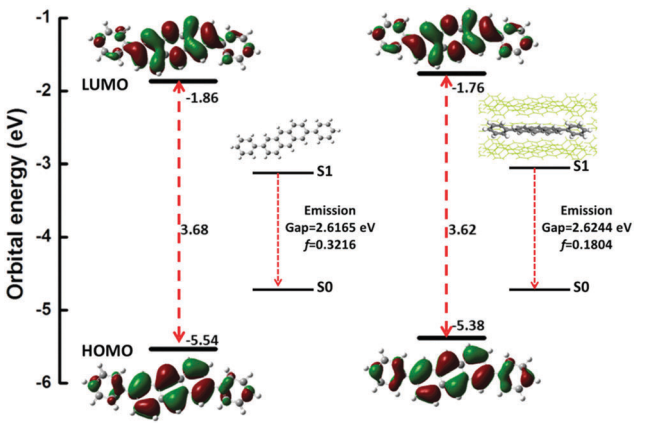

Fig. 3 Spatial distributions of HOMO and LUMO as well as their orbital energies for DPA in THF (left) and the solid phase (right) respectively. The emission energy and oscillator strength are shown as insets.

Table 1 The dihedral angles (θ_1 and θ_2) as well as the bond lengths (B_1 and B_2) of DPA marked in Fig. 1a, for the S0 and S1 states in THF and the solid phase are listed respectively

	THF			Solid		
Geometry	S0	S1	Δ	S0	S1	Δ
θ_1	36.2	26.6	9.6	18.7	16.2	2.5
θ_2	143.6	153.3	9.7	160.3	162.5	2.2
B_1	1.4791	1.4644	0.0147	1.4783	1.4621	0.0162
B_2	1.4791	1.4644	0.0147	1.4783	1.4621	0.0162

Table 2 The dihedral angles (θ_1–θ_4) as well as the bond lengths (B_1–B_5) of DP-BPEA marked in Fig. 1b, for the S0 and S1 states in THF and the solid phase are listed respectively

	THF			Solid		
Geometry	S0	S1	Δ	S0	S1	Δ
θ_1	35.6	32.3	3.3	28.9	27.2	1.7
θ_2	144.5	147.6	3.1	149.6	151.0	1.4
θ_3	179.6	179.8	0.2	175.4	175.9	0.5
θ_4	179.8	179.5	0.3	179.6	179.4	0.2
B_1	1.4785	1.4737	0.0048	1.4757	1.4685	0.0072
B_2	1.4785	1.4737	0.0048	1.4757	1.4685	0.0072
B_3	1.4208	1.4064	0.0144	1.4198	1.409	0.0106
B_4	1.2187	1.2290	0.0103	1.2184	1.2267	0.0083
B_5	1.4150	1.3903	0.0247	1.4145	1.3949	0.0196

change about 10° in THF, and have small variations of about 2° in the solid phase when the molecule transfers from S1 to S0. Thus, for DPA, the major geometry changes come from dihedral angle variations, and these changes can be limited by the rigid environment due to the influence of the intermolecular interaction in the solid phase. So, the nonradiative energy consumption path through the rotation of the dihedral angle is hindered and enhanced fluorescence efficiency can be expected. For more visualization, we calculated the rotational energy barriers by rotating the dihedral angle θ_1 of DPA in THF and in the solid phase. Here, the rotation angle is the dihedral angle after rotation minus the dihedral angle at the S0 structure, and then the resulting geometry after rotation is obtained by performing a constrained optimization from each starting conformation with the changed dihedral. Besides, the rotational energy barrier (kcal mol^{-1}) is acquired by the energy difference between the resulting configuration after rotation and the S0 geometry. The corresponding results are shown in Fig. 4. It can be clearly seen that the rotation energy barrier is much higher in solid phase than that in THF and this indicates the terminal phenyl ring is more rigid and not susceptible to rotate in the solid phase due to the restricted intramolecular rotation (RIR) effect. Therefore, the restricted rotation of the phenyl ring results in the smaller structural changes between S0 and S1 in the solid phase. As for DP-BPEA, the dihedral angle of θ_1–θ_4 almost remains unchanged either in THF or in the solid phase when the molecule transfers from S1 to S0, thus the changes of bond length (B_1–B_5) are highlighted. The vibrations of B_3, B_4 and B_5 are restricted by the enhanced intermolecular interaction in the solid phase, and no-remarkable geometry changes between S0 and S1 are observed for DP-BPEA from THF to the solid phase compared with DPA. Thus, the nonradiative energy consumption path is almost unaffected when the molecule transfers from THF to the solid phase because the effect of the restricted intramolecular vibration (RIV) is not as large as RIR,[27–29] thus a similar fluorescence efficiency can be expected in THF and the solid phase. More evidence will be shown in a later section.

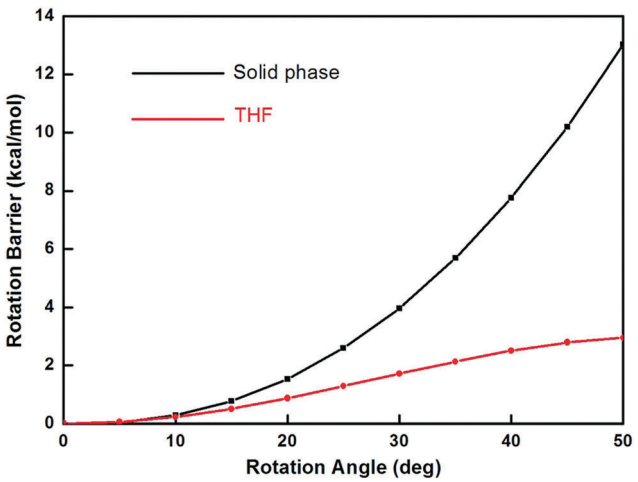

Fig. 4 Rotational energy barrier for DPA obtained by rotating the dihedral angle θ_1 marked in Fig. 1.

So, the additional phenylethynyl unit in DP-BPEA changes the molecular arrangement characteristic in the crystal and brings forth different mechanisms of RIR and RIV for DPA and DP-BPEA respectively, and this further affects the geometry changes and photophysical properties.

4.2 Huang–Rhys factor and reorganization energy in THF and solid phase

The Huang–Rhys factor and reorganization energy are two effective ways to measure the nonradiative consumption of excited state energy. The reorganization energy (λ) can be expressed as a summation of the contributions from normal mode (NM) relaxation in the harmonic oscillator approximation: $\lambda = \sum_k w_k \mathrm{HR}_k$ and $\mathrm{HR}_k = \frac{w_k D_k^2}{2\hbar}$. HR_k is the Huang–Rhys factor for the kth mode and D_k represents the displacement for the kth mode between S0 and S1. The values of the Huang–Rhys factor and reorganization energy can be obtained by the DUSHIN program. Then, the reorganization energy *versus* the normal mode frequencies and the Huang–Rhys factor *versus* the normal mode frequencies both in THF and the solid phase of the two studied molecules are plotted in Fig. 5 and 6. For DPA, it can be seen that the HR factors of DPA are much smaller in the solid phase (Fig. 5b) than these in THF (Fig. 5a) especially for the low frequency region (<500 cm^{-1}). Combined with the insets shown in Fig. 5(a), we know the low-frequency terminal phenyl ring rotations are hindered in the solid phase due to the intermolecular interaction and this result is consistent with the abovementioned analysis of geometry changes. Moreover, the calculated reorganization energy is 224.2 meV in THF whereas it decreases to 202.2 meV in the solid phase (Table 3). Although reorganization energies are all mainly contributed by bond stretching vibrations (insets in Fig. 5(c and d)), a remarkable reduction can be found in the low frequency region especially for the one at 53.77 cm^{-1}, and this mode corresponds to the rotation of the terminal phenyl rings (insets in Fig. 5c). Thus, the intermolecular interaction of DPA in the solid phase can efficiently restrict the intramolecular rotation of the terminal phenyl rings in the low frequency region. For DP-BPEA, HR factors almost remain unchanged in all regions with faint changes in the low frequency section especially for the mode of 54.89 cm^{-1} (insets in Fig. 6a). Besides, the calculated reorganization energy is 153.6 meV and 129.7 meV for THF and the solid phase (Table S3, ESI†) respectively. They are all mainly contributed by high frequency modes (>500 cm^{-1}). On detailed observation, we find that the reorganization energy contributed by the mode of 2305.53 cm^{-1} which is associated with –C≡C– stretching vibrations in the additional phenylethynyl, is decreased in the solid phase (mode 2307.06 cm^{-1}). This finding is consistent with the result in the former section: the vibrations of B_3, B_4 and B_5 are restricted by the enhanced intermolecular interaction in the solid phase.

To better clarify the relationship between the energy dissipation and the molecular geometry, the reorganization energies in THF and the solid phase are all projected onto the internal coordinate of the molecule, and the reorganization

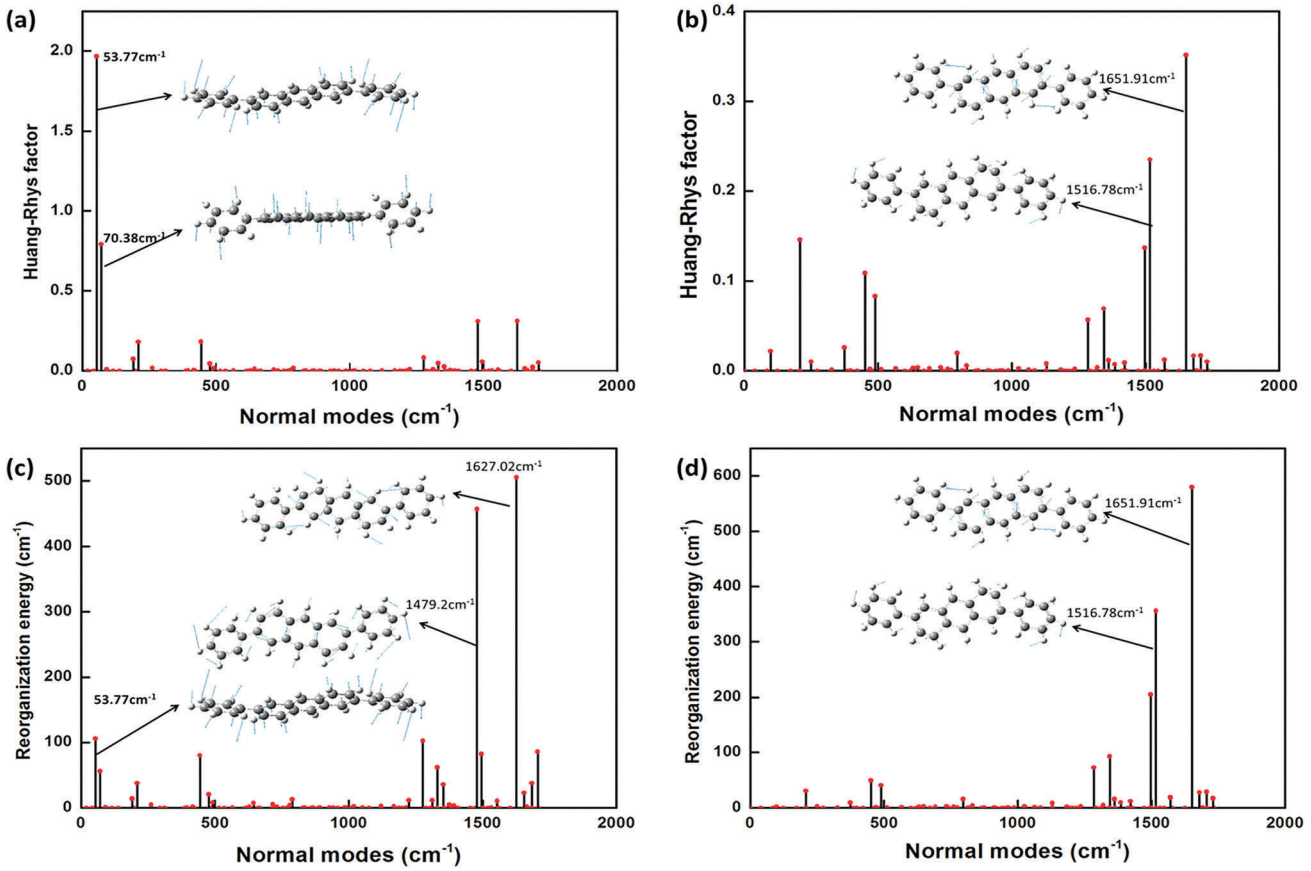

Fig. 5 Calculated HR factors *versus* the normal mode frequencies of DPA in THF (a) and in the solid phase (b) as well as reorganization energies *versus* the normal mode frequencies in THF (c) and the solid phase (d) respectively. Selected vibration modes are shown as insets.

energies contributed by the bond length, bond angle and dihedral angle are summarized in Fig. 7 (Fig. S4, ESI†) and the corresponding data are collected in Table 3 (Table S3, ESI†) for DPA (DP-BPEA). For DPA, It is noted that the contribution from the bond length accounts for the major contribution (85.3% in THF and 93.6% in solid phase) and this is consistent with the results shown in Fig. 5c and d. Besides, the contribution from the dihedral angle is 20.2 meV (9.0%) in THF, but it is decreased to 2.1 meV (1.0%) in the solid phase. The decreased reorganization energy (22 meV) from THF to the solid phase mainly comes from the decrement of the dihedral angle (18.1 meV) associated with the terminal phenyl ring rotations in low frequency regions. These results further confirm that the rotation motion of the terminal phenyl ring in the low frequency region is restricted, and the intermolecular interaction in the DPA crystal can affect the luminescent property. As for DP-BPEA, different phenomena are found. The contribution from the bond length also accounts for the major contribution (94.1% in THF and 94.4% in the solid phase), and the decreased reorganization energy from THF to solid ($\Delta_{\mathrm{THF-solid}}$ = 23.9 meV) associated with the high frequency regions is mainly contributed by the decrement of bond length (22.1 meV). All these data are consistent with the geometry changes in Section 4.1.

So, by a detailed analysis on the variation of HR and reorganization energy when the molecule transfers from THF to the solid phase, we know that the additional phenylethynyl unit changes the protagonist from the dihedral angle for DPA to the bond length for DP-BPEA, and this brings about different mechanisms of RIR and RIV for DPA and DP-BPEA respectively.

4.3 Quantum yield in THF and the solid phase

In order to quantify the energy consumption from the excited state to the ground state, we calculate the radiative decay rate and nonradiative decay rate by the method illustrated in the section ''Theoretical method'', and further we obtain the fluorescence quantum yield in THF and the solid phase respectively; all the data are listed in Table 4. For DPA, the radiative decay rate is 5.39×10^7 S^{-1} in the solid phase which is slightly decreased compared with the radiative decay rate in THF (9.55×10^7 S^{-1}), and this is because of the decreased oscillator strength although the vertical emission energy gap is increased in the solid phase (shown in Fig. 3). Besides, the nonradiative decay rate changes from 9.28×10^8 S^{-1} in THF to 4.02×10^7 S^{-1} in the solid phase, thus it brings about an enhanced fluorescence quantum yield from 9.33% in THF to 57.38% in the solid phase which is consistent with the experimental value (41.2%) measured in the single crystal. As for DP-BPEA, due to the additional phenylethynyl unit, the radiative decay rate retains an order of magnitude greater than that of DPA both in THF and the solid phase. Thus, a similar fluorescence quantum yield can be found for DP-BPEA

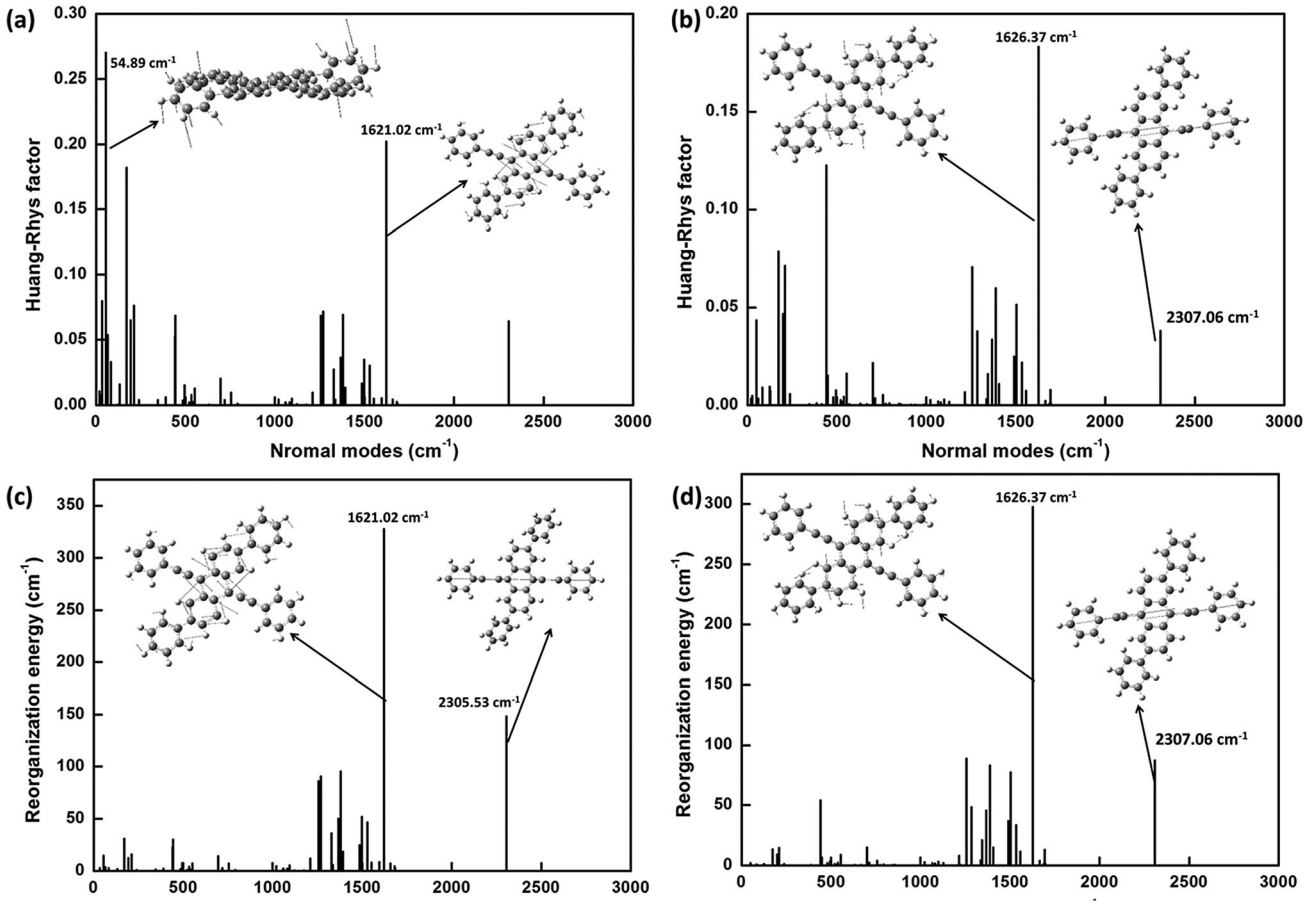

Fig. 6 Calculated HR factors *versus* the normal mode frequencies of DP-BPEA in THF (a) and in the solid phase (b) as well as the reorganization energies *versus* the normal mode frequencies in THF (c) and the solid phase (d) respectively. Selected vibration modes are shown as insets.

Table 3 Reorganization energies (meV) from the bond length, bond angle, and dihedral angle of DPA in THF and the solid phase are listed respectively

	THF	Solid	$\Delta_{\mathrm{THF-solid}}$
Bond length	191.3	189.2	2.1
Bond angle	12.7	10.9	1.8
Dihedral angle	20.2	2.1	18.1
Total	224.2	202.2	22.0

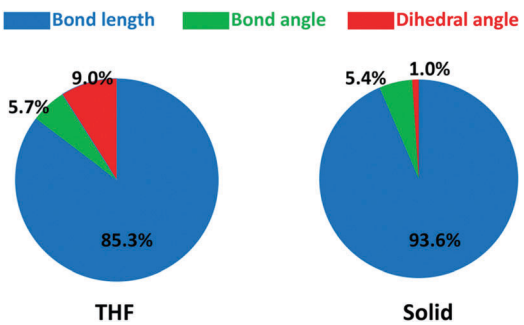

Fig. 7 Contributions to the reorganization energies from the bond length (blue), bond angle (green) and dihedral angle (red) of DPA in THF (left) and the solid phase (right).

in THF (58.58%) and in the solid phase (59.32%). This illustrates that the nonradiative energy consumption path is hardly hindered. To confirm the reliability of the nonradiative decay rate in our calculation, we plot the $\log K_{\mathrm{IC}}$ (ΔE (eV)) parabola in Fig. S5 and S6 (ESI†). No vibrational feature is found in both lines for the studied molecules, and this indicates the accuracy of the calculated K_{IC}.

So, the aggregation induced emission enhancement (AIEE) characteristic of DPA from THF to the solid phase is found, and this is mainly due to the restricted intramolecular rotation of terminal phenyl rings in low frequency regions. Moreover, the additional phenylethynyl unit can enhance the radiative decay rate, and the effect of RIV is not large as RIR, thus a similar fluorescence efficiency is found for DP-BPEA in THF and the solid phase. Our calculations show that the calculated non-radiative decay rates in solution by PCM are always larger than their real values, this usually brings about an underestimated PLQY theoretically. The reason is that the polarizable continuum model is difficult to properly describe the intermolecular interaction. In the solid phase, the QM/MM method is adopted, the exciton coupling effects *etc.* are not being included. These factors cause the disagreement between the experimentally measured efficiency and the theoretically computed value. These results indicate that different intermolecular interactions

Table 4 The calculated rate constants of radiative (k_r) and non-radiative (k_{IC}) from S1 to S0 in THF and the solid phase as well as their fluorescence efficiencies for DPA and DP-BPEA are listed respectively

	DPA		DP-BPEA	
Geometry	THF	Solid	THF	Solid
k_r (s^{-1})	9.55×10^7	5.39×10^7	1.57×10^8	1.06×10^8
k_{IC} (s^{-1})	9.28×10^8	4.02×10^7	1.11×10^8	7.27×10^7
Φ_F	9.33%	57.38%	58.58%	59.32%

can change the photophysical properties. Besides, for J-aggregation, the intermolecular arrangement becomes looser compared with that in H-aggregation, and this brings about a weak intermolecular exciton coupling which can be calculated as the Coulomb integral between transition densities of different molecules.[30,31] In this work, the intermolecular electrostatic interaction that dominates the photophysical properties is considered to demonstrate the J-aggregation effect on fluorescence efficiency.

4.4 Charge mobility

Based on the Marcus theory illustrated in the "Theoretical method" section, the charge transfer rate is calculated. An important factor which can influence the transfer rate is the transfer integral (V) which depends on the relative position of the two sites involved. Based on the X-ray crystal data, the charge transfer pathways are shown in Fig. 8. For DPA, the path of P1–P4 (at a distance of 4.823 Å) plays major roles with the maximum transfer integer being 57 meV and 37 meV for hole and electron transfer respectively. Due to the introduction of the phenylethynyl unit, the stacking mode is changed, only P1 and P2 (in distance of 3.932 Å) play leading roles with the transfer integer being 63 meV and 67 meV for the hole and electron transfer respectively. Besides, the formation of J-aggregation can be found in the crystal and this stacking mode can balance the contradiction between high mobility and efficient fluorescence emission. This provides a guideline for developing high mobility emissive organic semiconductors for OLEDs, OFETs and OLETs.

Based on the transfer rate, the charge mobility of both the hole and electron is calculated using the kinetic Monte Carlo simulation. The temperature dependence of the charge mobility is also investigated (shown in Fig. 9). One can see that the hole mobilities are all higher in value than the electron mobilities in the temperature ranging from 50 K to 300 K, which indicates that both the DPA and DP-BPEA molecular crystals are typical p-type organic semiconductors with the hole mobility up to 3.39 $cm^2\ V^{-1}\ s^{-1}$ and 1.62 $cm^2\ V^{-1}\ s^{-1}$ in 298 K respectively. Compared with DPA, a more balanced charge transfer can be seen for DP-BPEA due to the additional phenylethynyl unit which not only changes the photophysical characteristics but also regulates the charge transfer properties. Besides, both the hole and electron mobility increases with the temperature, which also confirms the hopping transfer mechanism of charges in the molecular crystal. More evidence, the calculated DPA reorganization energy of the hole (148 meV) and electron (206 meV) are all larger than their transfer integrals (57 meV for hole and 37 meV for electron), and the smaller hole reorganization

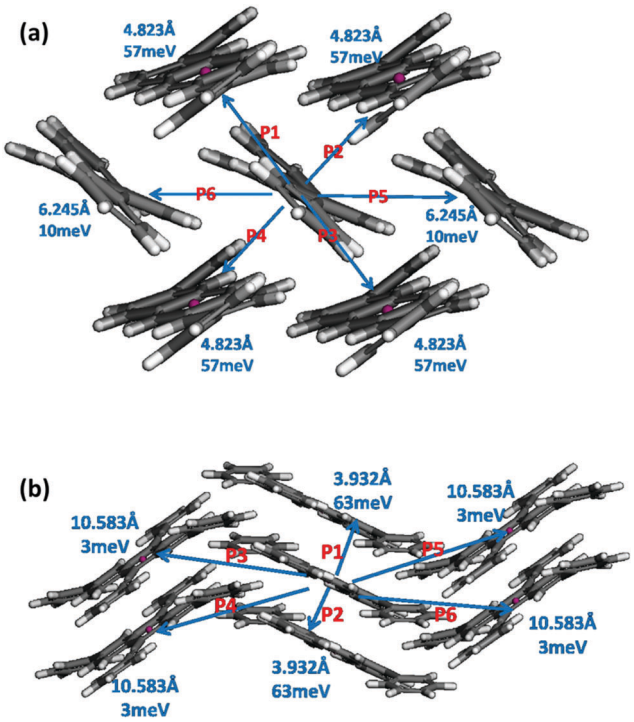

Fig. 8 Hole transfer pathways for DPA (a) and DP-BPEA (b) crystals respectively.

energy and larger hole transfer integral than these for electron means the hole mobility is larger than the electron mobility over all temperature ranges. However for the DP-BPEA, the reorganization energy of the electron (169 meV) is larger than that of the hole (133 meV) although the transfer integral of the hole (63 meV) is smaller than that of the electron (67 meV), and this brings about a larger hole mobility than electron mobility. One can regard the transfer integral as an 'attraction' and this attraction effect promotes the charge transfer between adjacent molecules, while the reorganization energy is considered as a 'pull' and this pull effect tends to constrain the charge in a single molecule. All these features $\left(\frac{du}{dT} > 0, \lambda \gg V\right)$ indicate a hopping mechanism for the DPA and DP-BPEA molecular crystals. Furthermore, a more balanced charge transfer can be found for DP-BPEA due to similar reorganization energy for hole and electron as well as a similar transfer integral for hole and electron than that for DPA.

Besides, the experimental mobility of DPA is as high as 34 $cm^2\ V^{-1}\ s^{-1}$ in the single crystal which is about 9 times larger than that of the calculated data, this is because many complex factors are neglected such as the electric field, the interface between the active layer and the charge carrier density. These factors also play important roles in the practical device and their effect on the charge transfer properties are more complicated when they are tangled together.[17,32,33] Thus, the differences between the theoretical results with the experimental data emerge. Besides, it should be noted that from both the mechanism and computational chemistry points of view, there are still important

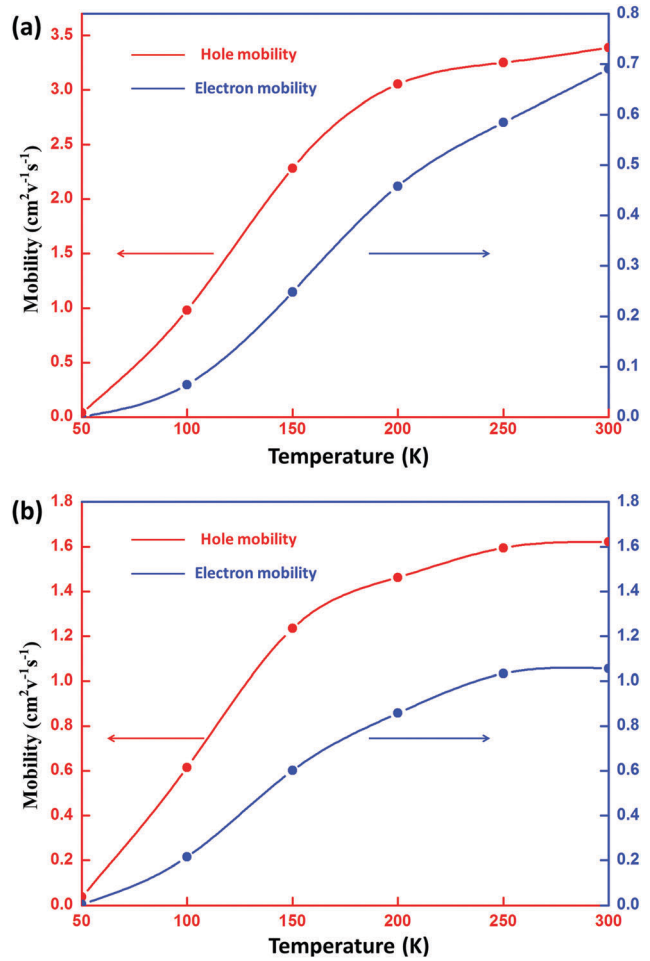

Fig. 9 Temperature dependence of charge mobility for DPA (a) and DP-BPEA (b) crystals respectively.

challenges in modelling the charge transport phenomena towards quantitative description and prediction.[34,35] In short, we are still a long way from a full understanding of the transport behavior in organic materials.

5. Conclusion

In summary, through a QM/MM method and kinetic Monte Carlo simulation, we investigate the photophysical and charge transfer properties of two high mobility emissive organic semiconductors DPA and DP-BPEA. The results show that, for DPA, the rotation motions of terminal phenyl ring are important in governing the photophysical properties, and these motions are effectively hindered in the solid phase. Thus, HR factors and reorganization energies are smaller in the solid phase compared with these in THF, nonradiative energy consumption pathways from the excited state to the ground state are suppressed by the RIR effect. Besides, the reorganization energy is mainly contributed by the bond length and the decreased reorganization energy from THF to the solid phase mainly comes from the decrement of the dihedral angle associated with terminal phenyl ring rotation, this brings about the AIEE characteristic of DPA with the calculated PLQY being 9.33% in THF and 57.38% in the solid phase respectively. For DP-BPEA, the reorganization energy from the bond length accounts for the major contribution, and the decreased reorganization energy from THF to solid is also mainly contributed by the decrement of bond length. As RIV is not as obvious as RIR, a similar fluorescence efficiency is obtained for DP-BPEA in THF solution and the solid phase. Furthermore, the DPA and DP-BPEA crystals are p-type semiconductors under the hopping transfer mechanism. Calculation confirms that the hole mobility of DPA (3.39 $cm^2 V^{-1} s^{-1}$) is larger than that of DP-BPEA (1.62 $cm^2 V^{-1} s^{-1}$) due to the number of effective transition pathways of DPA (four) being more than that of DP-BPEA (two). However a more balanced charge transfer can be found for DP-BPEA. Our theoretical work demonstrates the influence of molecular stacking of organic semiconductors on their photophysical and charger transfer properties, this could provide a guideline for developing more efficient high mobility emissive organic semiconductors for OLEDs, OFETs and OLETs.

Conflicts of interest

There are no conflicts of interest to declare.

Acknowledgements

This work is supported by the National Natural Science Foundation of China (Grant No. 11374195 and 21403133). Thanks are due to the support from the Taishan Scholar Project of Shandong Province and the Scientific Research Foundation of Shandong Normal University. Thanks are due to the support from the Promotive Research Fund for Excellent Young and Middle-aged Scientists of Shandong Province (Grant No. BS2014CL001) and the General Financial Grant from the China Postdoctoral Science Foundation (Grant No. 2014M560571). Great thanks are due to Professor Yi Luo, Professor Zhigang Shuai and Qian Peng for their helpful suggestions. Thanks are due to Professor Yingli Niu for his great help in the use of MOMAP and thanks to Professor Wenping Hu for providing the crystal data.

References

1 A. Hepp, H. Heil, W. Weise, M. Ahles, R. Schmechel and H. vonSeggern, *Phys. Rev. Lett.*, 2003, **91**, 157406.
2 T. Takenobu, S. Z. Bisri, T. Takahashi, M. Yahiro, C. Adachi and Y. Iwasa, *Phys. Rev. Lett.*, 2008, **100**, 066601.
3 M. Muccini, W. Koopman and S. Toffanin, *Laser Photonics Rev.*, 2012, **6**, 258.
4 R. Zhang, B. Li, M. C. Iovu, M. Jeffries-El, G. Sauvé, J. Cooper, S. Jia, S. Tristram-Nagle, D. M. Smilgies and D. N. Lambeth, *J. Am. Chem. Soc.*, 2006, **128**, 3480.
5 J. Guo, X. L. Li, H. Nie, W. Luo, S. Gan, S. Hu, R. Hu, A. Qin, Z. Zhao and S. J. Su, *Adv. Funct. Mater.*, 2017, **27**, 1606458.
6 F. Meng, C. Zhang, D. Chen, W. Zhu, H. L. Yip and S. J. Su, *J. Mater. Chem. C*, 2017, **5**, 6169.

7 J. Gibson, A. P. Monkman and T. J. Penfold, *ChemPhysChem*, 2016, **17**, 2956.
8 Y. Xie, Y. Ge, Q. Peng, C. Li, Q. Li and Z. Li, *Adv. Mater.*, 2017, **29**, 1606829.
9 M. Zambianchi, E. Benvenuti, C. Bettini, C. Zanardi, R. Seeber, D. Gentili, M. Cavallini, M. Muccini, V. Biondo and C. Soldano, *J. Mater. Chem. C*, 2016, **4**, 9411.
10 K. Oniwa, H. Kikuchi, H. Shimotani, S. Ikeda, N. Asao, Y. Yamamoto, K. Tanigaki and T. Jin, *Chem. Commun.*, 2016, **52**, 4800.
11 S. o. Kim, T. K. An, J. Chen, I. Kang, S. H. Kang, D. S. Chung, C. E. Park, Y. H. Kim and S. K. Kwon, *Adv. Funct. Mater.*, 2011, **21**, 1616.
12 B.-K. An, J. Gierschner and S. Y. Park, *Acc. Chem. Res.*, 2011, **45**, 544.
13 J. Liu, H. Zhang, H. Dong, L. Meng, L. Jiang, L. Jiang, Y. Wang, J. Yu, Y. Sun and W. Hu, *Nat. Commun.*, 2015, **6**, 10032.
14 J. Liu, J. Liu, Z. Zhang, C. Xu, Q. Li, K. Zhou, H. Dong, X. Zhang and W. Hu, *J. Mater. Chem. C*, 2017, **5**, 2519.
15 J. Fan, L. Cai, L. Lin and C.-K. Wang, *J. Phys. Chem. A*, 2016, **120**, 9422.
16 L. Wang, Q. Li, Z. Shuai, L. Chen and Q. Shi, *Phys. Chem. Chem. Phys.*, 2010, **12**, 3309.
17 L. Lin, H. Geng, Z. Shuai and Y. Luo, *Org. Electron.*, 2012, **13**, 2763.
18 Z. Shuai and Q. Peng, *Phys. Rep.*, 2014, **537**, 123.
19 Q. Peng, Y. Yi, Z. Shuai and J. Shao, *J. Chem. Phys.*, 2007, **126**, 114302.
20 Y. Niu, Q. Peng and Z. Shuai, *Sci. China, Ser. B: Chem.*, 2008, **51**, 1153.
21 Z. Shuai, H. Geng, W. Xu, Y. Liao and J.-M. André, *Chem. Soc. Rev.*, 2014, **43**, 2662.
22 M. J. Frisch, G. W. Trucks, H. B. Schlegel, G. E. Scuseria, M. A. Robb, J. R. Cheeseman, G. Scalmani, V. Barone, B. Mennucci, G. A. Petersson, H. Nakatsuji, M. Caricato, X. Li, H. P. Hratchian, A. F. Izmaylov, J. Bloino, G. Zheng, J. L. Sonnenberg, M. Hada, M. Ehara, K. Toyota, R. Fukuda, J. Hasegawa, M. Ishida, T. Nakajima, Y. Honda, O. Kitao, H. Nakai, T. Vreven, J. A. Montgomery, Jr., J. E. Peralta, F. Ogliaro, M. Bearpark, J. J. Heyd, E. Brothers, K. N. Kudin, V. N. Staroverov, R. Kobayashi, J. Normand, K. Raghavachari, A. Rendell, J. C. Burant, S. S. Iyengar, J. Tomasi, M. Cossi, N. Rega, J. M. Millam, M. Klene, J. E. Knox, J. B. Cross, V. Bakken, C. Adamo, J. Jaramillo, R. Gomperts, R. E. Stratmann, O. Yazyev, A. J. Austin, R. Cammi, C. Pomelli, J. W. Ochterski, R. L. Martin, K. Morokuma, V. G. Zakrzewski, G. A. Voth, P. Salvador, J. J. Dannenberg, S. Dapprich, A. D. Daniels, O. Farkas, J. B. Foresman, J. V. Ortiz, J. Cioslowski and D. J. Fox, *Gaussian09 Revision A.01*, Gaussian Inc., Wallingford CT, 2009.
23 M. Rätsep, Z.-L. Cai, J. R. Reimers and A. Freiberg, *J. Chem. Phys.*, 2011, **134**, 01B608.
24 H. Ma, W. Shi, J. Ren, W. Li, Q. Peng and Z. Shuai, *J. Phys. Chem. Lett.*, 2016, **7**, 2893.
25 Y. Niu, Q. Peng, C. Deng, X. Gao and Z. Shuai, *J. Phys. Chem. A*, 2010, **114**, 7817.
26 Q. Peng, Q. Shi, Y. Niu, Y. Yi, S. Sun, W. Li and Z. Shuai, *J. Mater. Chem. C*, 2016, **4**, 6829.
27 N. L. Leung, N. Xie, W. Yuan, Y. Liu, Q. Wu, Q. Peng, Q. Miao, J. W. Lam and B. Z. Tang, *Chem. – Eur. J.*, 2014, **20**, 15349.
28 G. Yu, S. Yin, Y. Liu, J. Chen, X. Xu, X. Sun, D. Ma, X. Zhan, Q. Peng, Z. Shuai, B. Tang, D. Zhu, W. Fang and Y. Luo, *J. Am. Chem. Soc.*, 2005, **127**, 6335.
29 S. Yin, Q. Peng, Z. Shuai, W. Fang, Y.-H. Wang and Y. Luo, *Phys. Rev. B: Condens. Matter Mater. Phys.*, 2006, **73**, 205409.
30 W. Li, Q. Peng, Y. Xie, T. Zhang and Z. Shuai, *Acta Chim. Sin.*, 2016, **74**, 902.
31 W. Li, L. Zhu, Q. Shi, J. Ren, Q. Peng and Z. Shuai, *Chem. Phys. Lett.*, 2017, **683**, 507.
32 S. Yin and Y. Lv, *Org. Electron.*, 2008, **9**, 852.
33 S. Yin, Y. Yang and Y. Lv, *Synth. Met.*, 2010, **160**, 1241.
34 Z. Shuai, W. Xu, Q. Peng and H. Geng, *Sci. China: Chem.*, 2013, **56**, 1277.
35 A. Troisi, *J. Chem. Phys.*, 2011, **134**, 034702.

